The cellular NMD pathway restricts Zika virus infection and is targeted by the viral capsid protein

Krystal A. Fontaine[a], Kristoffer E. Leon[a,b], Mir M. Khalid[a], Sakshi Tomar[a], David Jimenez-Morales[a,c]*, Mariah Dunlap[a], Julia A. Kaye[a], Priya S. Shah[c]*, Steve Finkbeiner[a,d], Nevan J. Krogan[a,c] and Melanie Ott[a,e]#

[a]Gladstone Institutes, San Francisco, CA

[b]Medical Scientist Training Program, University of California, San Francisco, CA

[c]Quantitative Biology Institute, Department of Cellular and Molecular Pharmacology, University of California, San Francisco, CA

[d]Department of Neurology and Physiology, University of California, San Francisco, CA,

[e]Department of Medicine, University of California, San Francisco, CA

Running title: Zika virus capsid protein targets the NMD pathway

#Address correspondence to Melanie Ott, melanie.ott@gladstone.ucsf.edu.

*Present address: Priya S. Shah, Departments of Chemical Engineering and Microbiology and Molecular Genetics, University of California, Davis, CA.

David Jimenez-Morales, PhD, Department of Medicine, Division of Cardiovascular Medicine, Stanford University.

K.A.F and K.E.L contributed equally to this work.

Abstract word count: 198 | Text word count: 4,426

Abstract

Zika virus (ZIKV) infection of neural progenitor cells (NPCs) *in utero* is associated with neurological disorders, such as microcephaly, but a detailed molecular understanding of ZIKV-induced pathogenesis is lacking. Here we show that *in vitro* ZIKV infection of human cells, including NPCs, causes disruption of the nonsense-mediated mRNA decay (NMD) pathway. NMD is a cellular mRNA surveillance mechanism that is required for normal brain size in mice. Using affinity purification-mass spectrometry, we identified multiple cellular NMD factors that bind to the viral capsid protein, including the central NMD regulator up-frameshift protein 1 (UPF1). Endogenous UPF1 interacted with the ZIKV capsid protein in co-immunoprecipitation experiments, and capsid expression post-transcriptionally downregulated UPF1 protein levels, a process that we confirmed occurs during ZIKV infection. Cellular fractionation studies show that the ZIKV capsid protein specifically targets nuclear UPF1 for degradation via the proteasome. A further decrease in UPF1 levels by RNAi significantly enhanced ZIKV infection in NPC cultures, consistent with a model in which NMD restricts ZIKV infection in the fetal brain. We propose that ZIKV, via the capsid protein, has evolved a strategy to lower UPF1 levels and dampen antiviral activities of NMD, which in turn contributes to neuropathology *in vivo.*

44 **Importance**

45 Zika virus (ZIKV) is a significant global health threat, as infection has been linked to
46 serious neurological complications, including microcephaly. Using a human stem cell-
47 derived neural progenitor model system, we find that a critical cellular quality control
48 process called the nonsense-mediated mRNA decay (NMD) pathway is disrupted during
49 ZIKV infection. Importantly, disruption of the NMD pathway is a known cause of
50 microcephaly and other neurological disorders. We further identify an interaction between
51 the capsid protein of ZIKV and up-frameshift protein 1 (UPF1), the master regulator of
52 NMD, and show that ZIKV capsid targets UPF1 for degradation. Together, these results
53 offer a new mechanism for how ZIKV infection can cause neuropathology in the
54 developing brain.

55

56

57 **Introduction**

58 ZIKV is a mosquito-borne RNA virus that belongs to the *Flaviviridae* family. First
59 isolated in Uganda in 1947, ZIKV remained relatively obscure for decades following its
60 discovery because infection was associated with only mild disease. However, more
61 severe clinical manifestations, including microcephaly, have been observed during the
62 recent spread of ZIKV through the Americas (1). ZIKV infection induces cell cycle arrest
63 and apoptosis in neural progenitor cells (NPCs) in *in vitro* studies and *in vivo* mouse
64 models, with the latter resulting in cortical thinning and microcephaly (2-6). While it is now
65 established that ZIKV infection during pregnancy is a causative agent of microcephaly
66 (7), the molecular mechanisms underlying ZIKV-induced neuropathogenesis remain
67 largely unknown.

68 Similar to other flaviviruses, ZIKV contains a single-stranded, positive-sense RNA
69 genome of ~11 kb in size. The genome encodes a single polyprotein that is post-
70 translationally processed by both host and viral proteases to produce 3 structural and 7
71 nonstructural proteins (8, 9). The flavivirus capsid, which is the first protein encoded in
72 the genome, is a major structural element required for the encapsidation of the RNA
73 genome during virion assembly (10). While flavivirus replication is known to occur in the
74 cytoplasm, a significant portion of the viral capsid protein localizes to the nucleus during
75 infection (10, 11). Although the role of nuclear capsid during infection is less clear, several
76 functions have been suggested. The capsid protein from dengue virus, a close relative of
77 ZIKV, binds to core histones and inhibits nucleosome formation, thus implicating the
78 protein in altering host gene expression (12). Furthermore, several flavivirus capsid

79 proteins, including ZIKV capsid, localize to the nucleolus, with many interacting with
80 nucleolar proteins to promote viral particle production (13-16).

81 The nonsense-mediated mRNA decay (NMD) pathway was initially discovered as
82 a highly conserved quality control system that destroys transcripts containing premature
83 termination codons (PTCs)(17). Following splicing of pre-mRNAs, a multi-subunit protein
84 complex called the exon-junction complex (EJC) is deposited onto mRNAs near the sites
85 of exon-exon junctions. If a PTC is found ~50–55 nucleotides upstream of an EJC, the
86 mRNA will be subjected to NMD-mediated degradation initiated by the recruitment of the
87 RNA helicase up-frameshift protein 1 (UPF1). UPF1 plays a central role in the NMD
88 pathway by linking the translation termination event to the assembly of a surveillance
89 complex, resulting in NMD activation (18). Interestingly, microcephaly has been
90 associated with genetic mutations that result in the impairment of the NMD pathway.
91 While knockout of Upf1 and other NMD factors is embryonic lethal in mice (19), mice
92 haploinsufficient for the EJC components Magoh, Rbm8a, and Eif4a3 exhibit aberrant
93 neurogenesis and microcephaly (20-22).

94 In addition to PTC-containing transcripts, it is now known that the NMD pathway
95 recognizes a broader range of RNA substrates. Notably, the NMD controls the “normal”
96 expression of ~10% of the cellular transcriptome and is regarded as a post-transcriptional
97 mechanism of gene regulation (23). Furthermore, the NMD pathway also regulates viral
98 infections. While it was first reported that UPF1 promotes the infectivity of HIV-1 progeny
99 virions (24), replication of several human RNA viruses, including human T-cell
100 lymphotropic virus type 1 (HTLV-1), Semliki Forest virus and Sindbis virus, is enhanced

101 following UPF1 knockdown, implicating UPF1 and the NMD pathway, either directly or
102 indirectly, in the host antiviral response (25-28). As ZIKV infection and NMD impairment
103 both promote microcephaly development, and we previously described disruption of the
104 NMD pathway in cells infected with a related flavivirus, the hepatitis C virus (HCV) (29),
105 we hypothesized that ZIKV infection manipulates the cellular NMD pathway, a process
106 contributing to ZIKV-induced neuropathology.
107
108 **Results**
109
110 **The NMD pathway is impaired during ZIKV infection.** To determine if ZIKV infection
111 affects NMD, we infected human hepatoma cells (Huh7) and human induced pluripotent
112 stem cell (iPSC)-derived NPCs with ZIKV for 48 h. We isolated total RNA from infected
113 cells and measured mRNA levels of three canonical NMD substrates: asparagine
114 synthetase (ASNS), cysteinyl-tRNA synthetase (CARS), and SR protein SC35 (29).
115 ASNS, CARS, and SC35 transcripts were significantly elevated in Huh7 cells and NPCs
116 following infection with Asian lineage ZIKV strain P6-740 (Fig. 1a). Levels of NMD
117 substrates were also elevated in Huh7 cells infected with the contemporary ZIKV clinical
118 isolate PRVABC59 (Puerto Rico, 2015) (Fig. 1a). We found that the ZIKV-induced
119 increase in NMD transcripts did not reflect a global increase in transcription, as mRNA
120 levels of housekeeping genes, including glyceraldehyde 3-phosphate dehydrogenase
121 (GAPDH), were not altered in infected cells (Fig. 1a). Together, these results indicate that
122 the NMD pathway is impaired in ZIKV-infected cells.

123 NMD substrates are regulated through the ATP-dependent RNA helicase activity
124 of UPF1, the central regulator of NMD (18). To determine if ZIKV infection broadly affects
125 NMD, we utilized two publicly available RNA sequencing (RNA-Seq) datasets to compare
126 genome-wide transcriptional alterations found during ZIKV infection (6) to those found
127 following UPF1 knockdown (30). As shown in Figure 1b, there is a significant overlap in
128 upregulated genes between these two datasets. Interestingly, several of the overlapping
129 genes are canonical NMD substrates (31-35) involved in cell cycle arrest and induction
130 of apoptosis, two conditions linked to ZIKV-associated neuropathology (5). These genes
131 include DNA damage-inducible transcript 3 (DDIT3) (36) and growth arrest and DNA
132 damage-inducible protein 45 alpha and beta (GADD45A and GADD45B, respectively)
133 (37). Via quantitative real-time RT-PCR, we confirmed that transcripts of each were
134 upregulated following infection of Huh7 cells with ZIKV PRVABC59, while the mRNA
135 levels of the housekeeping genes GAPDH, hypoxanthine phosphoribosyltransferase 1
136 (HPRT1), and lactate dehydrogenase A (LDHA) were not elevated (Fig. 1c). Combined,
137 these data show that ZIKV infection is associated with dysregulated expression of NMD
138 substrates relevant to ZIKV-mediated neuropathogenesis.
139
140 **ZIKV capsid interacts with the NMD pathway.** We previously showed that the core
141 protein of HCV, as well as the capsid protein of the related flaviviruses dengue virus and
142 West Nile virus, interact with the host protein within bgcn homolog (WIBG/PYM1), an EJC
143 disassembly factor associated with NMD (29, 38). To examine potential interactions
144 between ZIKV and the NMD pathway, we separately analyzed data generated from an

145 affinity purification-mass spectrometry (AP-MS) screen to specifically query whether the
146 capsid protein of ZIKV interacts with NMD-associated host factors (Shah et al.,
147 submitted). ZIKV-host protein-protein interaction (PPI) maps were generated in HEK293T
148 cells using ZIKV proteins from the Ugandan 1947 strain MR 766 or the French Polynesian
149 2013 strain H/PF/2013 as bait proteins.

150 From this analysis, we found that ZIKV capsid proteins interacted with several
151 components of the NMD pathway, including multiple members of the EJC complex, as
152 well as UPF1 and UPF3B, the latter an NMD effector that stimulates UPF1 helicase
153 activity (Fig. 2a) (39). Importantly, the NMD host factors that interacted with each of the
154 two different capsid proteins greatly overlapped, revealing that the interaction between
155 capsid and the NMD pathway is conserved across the Asian and African lineages of ZIKV
156 (Fig. 2a). Next, we validated the binding of ZIKV capsid to select NMD host factors by co-
157 immunoprecipitating FLAG-tagged capsid protein with endogenous UPF3B or UPF1 in
158 HEK293T cells. Both UPF3B and UPF1 proteins co-immunoprecipitated with ZIKV
159 capsid, thus confirming the AP-MS results (Fig. 2b,c, respectively). UPF1 interacted with
160 the viral capsid protein independently from its RNA-binding and ATPase/helicase
161 capacities, as ZIKV capsid co-immunoprecipitated with UPF1 mutants deficient in these
162 functions following overexpression (Fig 2d).

163

164 **ZIKV capsid degrades UPF1, the master regulator of NMD.** Surprisingly, we
165 consistently observed a decrease in UPF1, but not UPF3B, protein levels in the input
166 lysate of ZIKV capsid-transfected cells, pointing to a specific perturbation of endogenous

167 UPF1 expression by ZIKV capsid (Fig. 2c). To confirm that UPF1 protein levels are
168 dysregulated during ZIKV infection, we performed western blot analysis of infected Huh7
169 cells and NPCs. Cellular UPF1 protein levels were consistently downregulated by ~50%
170 in ZIKV-infected Huh7 cells, whereas a ~25% reduction was observed in ZIKV-infected
171 NPCs (Fig. 2e), mirroring the difference in infection efficiencies achieved in these two cell
172 systems. UPF1 transcript levels were not decreased in ZIKV-infected cells or following
173 ZIKV capsid overexpression, indicating that UPF1 is post-transcriptionally downregulated
174 during ZIKV infection (Supplemental Fig. 1a,b, respectively).

175 Because ZIKV capsid and UPF1 both localize to the nucleus and the cytoplasm
176 (13, 40) we performed fractionation studies in ZIKV capsid-transfected HEK293T cells to
177 determine if UPF1 is downregulated within a specific cellular compartment. Capsid
178 expression markedly decreased nuclear UPF1 levels, whereas cytoplasmic levels were
179 unchanged (Fig. 3a). We next examined a potential role for the autophagic and
180 proteasomal pathways, both of which are known to mediate nuclear protein degradation,
181 in ZIKV capsid-induced UPF1 downregulation. As shown in Supplemental Figure 2,
182 nuclear UPF1 levels in ZIKV capsid-transfected cells were not rescued by inhibition of
183 cellular autophagy via bafilomycin A1 treatment. However, nuclear UPF1 levels were
184 restored in a dose-dependent manner following treatment with the proteasome inhibitor
185 bortezomib (Fig. 3b), indicating enhanced proteasomal degradation of nuclear UPF1 in
186 the presence of ZIKV capsid. Although ZIKV capsid colocalized with endogenous UPF1
187 in the cytoplasm of transfected Huh7-Lunet cells (Mander's colocalization coefficient of
188 ~57%), we detected very little colocalization within the nucleus (~7%) (Supplemental

189 Figure 3). We hypothesized that this was due to specific degradation of UPF1 by ZIKV
190 capsid in the nucleus. Indeed, when cells were treated with bortezemib, the fraction of
191 nuclear UPF1 colocalizing with ZIKV capsid increased ~8-fold, while the fraction of
192 nuclear capsid interacting with UPF1 remained unchanged (Figure 3c). These results
193 demonstrate that ZIKV capsid interacts with UPF1 both in the cytoplasm and nucleus, but
194 specifically targets nuclear UPF1 for proteasomal degradation.
195
196 **UPF1 is a restriction factor of ZIKV.** To test the effect of lowered UPF1 levels on ZIKV
197 infection, we further decreased UPF1 expression prior to ZIKV infection by transfecting
198 NPCs with either non-targeting siRNA or a pool of UPF1-specific siRNAs. We then
199 infected the transfected cells with ZIKV and measured viral RNA levels, as well as
200 infectious titers, 48 h post-infection (hpi). UPF1 knockdown was successful in siRNA-
201 treated cells, as confirmed by western blot analysis (Fig. 4a). The depletion of UPF1 in
202 NPCs prior to infection resulted in a significant increase in both ZIKV RNA levels and
203 infectious virus production (Fig. 4b,c, respectively), indicating that expression of UPF1
204 restricts ZIKV infection at or before the RNA replication stage. To differentiate between
205 these two stages, we analyzed double-stranded RNA (dsRNA) intermediates
206 representing presumed viral RNA replication centers in infected NPCs (Fig. 4d)(41).
207 Using confocal microscopy and 3D reconstruction analyses, we observed no significant
208 difference in the number and size of dsRNA foci per cell when comparing ZIKV-infected,
209 UPF1-depleted NPCs to ZIKV-infected cultures expressing UPF1 (Fig. 4e,f). Instead, we
210 found a significant increase in the number of infected cells in NPC cultures when UPF1

211 was depleted, indicating that UPF1 regulates permissivity of NPCs to ZIKV infection at an
212 early stage prior to viral RNA replication (Fig. 4g).
213
214 **Discussion**
215 In summary, we identified the NMD pathway as a restriction mechanism for ZIKV
216 infection in human NPCs. NMD was partially inactivated in ZIKV-infected NPCs through
217 expression of the viral capsid protein and the resulting degradation of host nuclear UPF1.
218 As further weakening NMD by depleting UPF1 resulted in a marked increase in the
219 number of infected cells, we propose a model in which an evolutionary "arms race"
220 between cellular NMD and ZIKV determines whether a cell is successfully infected
221 (Fig.4h).
222 Downregulation of UPF1 by ZIKV capsid is not complete, and is likely limited by
223 the damaging effects of NMD disruption, as illustrated by the upregulation of genes
224 involved in cell growth arrest and apoptosis. Indeed, knockout of UPF1 and other
225 members of the NMD pathway is embryonic lethal in mice (19). However, mice
226 haploinsufficient for NMD factors upstream of UPF1, including Magoh, Rbm8a, and
227 Eif4a3, develop microcephaly (20-22). Thus, the reduction in nuclear UPF1 we observe
228 in ZIKV-infected NPCs could contribute to the microcephaly phenotype caused by ZIKV
229 infection in the fetal brain. While fetal and adult NPCs appear to be transcriptionally
230 distinct (42), it has been shown that adult NPCs are also permissive to ZIKV infection
231 (43). As the NMD pathway is a ubiquitous cellular surveillance mechanism, it is likely that
232 ZIKV capsid targets UPF1 for degradation in any cell type that is susceptible to ZIKV

233 infection. Accordingly, we have found that UPF1 is degraded following infection of both
234 NPCs and hepatic Huh7 cells.

235 Why ZIKV capsid specifically downregulates nuclear UPF1, and how nuclear UPF1
236 contributes to ZIKV restriction remain unanswered. Several studies suggest that NMD is
237 associated with the nucleus, although this issue remains controversial. Multiple
238 transcripts, such as those encoding T cell receptor beta, triosephosphate isomerase and
239 mouse major urinary protein, have been shown to be specifically degraded in purified
240 nuclei or reduced in nuclear fractions (44). These data support the model that selectively
241 depleting nuclear UPF1 levels disrupts NMD function in ZIKV-infected cells. In addition,
242 UPF1 is involved in several other processes within the nucleus, including nuclear-
243 associated RNA metabolism, cell cycle progression, and DNA replication (40). Therefore,
244 by targeting nuclear UPF1, ZIKV could disrupt these processes and program target cells
245 for viral replication. Notably, viral RNA replication is thought to occur solely within the
246 cytoplasmic compartment (45, 46). Using confocal microscopy and 3D reconstruction, we
247 did not detect dsRNA foci localized within the nuclei of ZIKV-infected cells (data not
248 shown), supporting our finding that UPF1 does not restrict viral RNA replication. While
249 our results suggest a role for nuclear UPF1 in ZIKV restriction, it is possible that UPF1
250 also serves as a restriction factor of ZIKV within the cytoplasm. Previously, it was shown
251 that UPF1 suppresses alphavirus replication by degrading the incoming viral RNA
252 following uncoating in the cytosol (28). Thus, ZIKV may possess an additional mechanism
253 to prevent cytoplasmic UPF1 from targeting its incoming RNA genome for destruction.

254 Our data reveal that nuclear UPF1 is degraded by ZIKV capsid in a proteasome-
255 dependent manner. While the nuclear proteasome has not been specifically linked to
256 microcephaly, it plays critical roles in the regulation of chromatin structure, gene
257 expression, DNA repair, and protein quality control (47). Thus, the co-opting of the nuclear
258 proteasome by ZIKV capsid to degrade UPF1 could disrupt its normal proteasomal
259 activity and further contribute to the cytopathic effects associated with ZIKV infection.
260 Furthermore, given that the capsid protein of the closely related dengue virus can
261 translocate across cell membranes (48), it is possible that capsid released from apoptotic,
262 ZIKV-infected cells can enter neighboring, uninfected cells to degrade UPF1, thus
263 increasing permissivity of bystander cells to ZIKV infection. Studies are ongoing to
264 determine the precise molecular mechanism of ZIKV capsid-mediated UPF1 degradation
265 and how UPF1 depletion enhances ZIKV replication, directly or indirectly. Ultimately,
266 these data may help inform new therapeutic approaches, as reinforcement of the antiviral
267 properties of the NMD pathway is expected to enhance resistance of NPCs to ZIKV
268 infection and to promote normal neurodevelopment in infected fetuses.
269

270 **Materials and Methods**

271 **Viruses and cells.** Two Asian lineage strains of ZIKV, P6-740 (ATCC VR-1845) and
272 PRVABC59 (ATCC VR-1843), were used for all experiments. ZIKV stocks were
273 propagated in Vero cells (ATCC) and titers were determined by plaque assays on Vero
274 cells. Huh7 cells (ATCC), Huh7-Lunet cells (Ralf Bartenschlager, Heidelberg University)
275 and Vero cells were maintained in Dulbecco's Modified Eagle's Medium (DMEM) with

276 10% fetal bovine serum (FBS), 2 mM L-glutamine, 100 U/mL penicillin, and 100 µg/mL
277 streptomycin. HEK293T cells (ATCC) were maintained in DMEM/H21 medium
278 supplemented with 10% FBS, 100 U/mL penicillin, 100 µg/mL streptomycin, and 1 mM
279 sodium pyruvate or DMEM with 10% FBS, 2 mM L-glutamine, 100 U/mL penicillin, and
280 100 µg/mL streptomycin. Human iPSC-derived NPCs were generated and maintained
281 as described previously (49). All of the human fibroblast cell lines used to generate iPSCs
282 came from the Coriell Institute for Medical Research and Yale Stem Cell Center. The
283 iPSCs used in these studies were the CTRL2493nXX, CS2518nXX, and Cs71iCTR-
284 20nXX lines. CTRL2493nXX was derived from the parental fibroblast line ND31845 that
285 was biopsied from a healthy female at 71 years of age. CS2518nXX was derived from the
286 parental fibroblast line ND30625 that was biopsied from a healthy male at 76 years of
287 age. CS71iCTR-20nXX was derived from the parental fibroblast line ND29971 that was
288 biopsied from a female at 61 years of age. For virus infections, NPCs plated on Matrigel-
289 coated (Corning) multi-well plates or Huh7 cells were infected with ZIKV at a multiplicity
290 of infection (MOI) of 0.1 or 1 for 2 h at 37°C. Infected cells were harvested at 48 hpi for
291 all analyses.
292
293 **Affinity purification, mass spectrometry, and AP-MS scoring.** The ZIKV capsid open
294 reading frames (ORFs) from the Ugandan 1947 strain MR 766 or the French Polynesian
295 2013 strain H/PF/2013 were cloned into pCDNA4_TO with a C-terminal 2xStrep II affinity
296 tag for expression in human cells. The viral capsid proteins (three biological replicates),
297 as well as GFP (two biological replicates) and empty vector (ten biological replicates) as

298 negative controls, were expressed in HEK293T cells and affinity purifications were
299 performed as previously described (50). Briefly, clarified lysates were incubated with
300 Strep-Tactin Superflow (IBA) overnight at 4°C. Proteins were eluted with 50 mM Tris pH
301 7.5, 150 mM NaCl, 1 mM EDTA containing 2.5 mM Desthiobiotin (IBA) for 30 min at 4°C.
302 Lysates and affinity purified eluates were analyzed by western blot and silver stain PAGE
303 to confirm expression and purification. Purified protein eluates were digested with trypsin
304 for LC-MS/MS analysis. Samples were denatured and reduced in 2M urea, 10 mM
305 NH_4HCO_3, 2 mM DTT for 30 min at 60°C, then alkylated with 2 mM iodoacetamide for 45
306 min at room temperature. Trypsin (Promega) was added at a 1:100 enzyme:substrate
307 ratio and digested overnight at 37°C. Following digestion, samples were concentrated
308 using C18 ZipTips (Millipore) according to the manufacturer's specifications. Peptides
309 were resuspended in 15 µL of 4% formic acid and 3% ACN, and 1-2 µL of sample was
310 loaded onto a 75 µm ID column packed with 25 cm of Reprosil C18 1.9 µm, 120Å particles
311 (Dr. Maisch GmbH). Peptides were eluted into a Q-Exactive Plus (Thermo Fisher) mass
312 spectrometer by gradient elution delivered by an Easy1200 nLC system (Thermo Fisher).
313 The gradient was from 4.5% to 32% acetonitrile over 53 min. All MS spectra were
314 collected with oribitrap detection, while the 20 most abundant ions were fragmented by
315 higher energy collisional dissociation (HCD) and detected in the orbitrap. All data was
316 searched against the SwissProt Human protein sequences, combined with ZIKV
317 sequences and GFP. Peptide and protein identification searches, as well as label-free
318 quantitation, were performed using the MaxQuant data analysis algorithm and all peptide
319 and protein identifications were filtered to a 1% false-discovery rate (51, 52). SAINTq (53)

320 was used to calculate the probability of bait-prey interactions for both Ugandan ZIKV
321 capsid and French Polynesian ZIKV capsid against the negative controls, including GFP
322 and empty vector, with protein intensities as input values. We applied a combined
323 threshold of probability of interaction (AvgP) greater than 0.90 and Bayesian False
324 Discovery Rate of less than 0.05.
325
326 **Quantitative real-time reverse transcription-PCR (qRT-PCR).** Total cellular RNA was
327 isolated from Huh7 cells and NPCs using the RNeasy Mini Kit (Qiagen). cDNA was
328 synthesized with oligo$(dT)_{18}$ (ThermoFisher Scientific) primers, random hexamer (Life
329 Technologies) primers, and AMV reverse transcriptase (Promega). The cDNA was then
330 used in SYBR Green PCR Master Mix (ThermoFisher Scientific) according to
331 manufacturer's instructions and analyzed by qPCR (Bio-Rad ABI 7900). The primers used
332 for ASNS, CARS, SC35 1.7, GAPDH, HPRT1, LDHA, and 18S rRNA have been
333 described previously (29). The additional primers used were ZIKV PRVABC59 forward
334 primer 5'- GAG ACG AGA TGC GGT ACA GG -3', ZIKV PRVABC59 reverse primer 5'-
335 CGA CCG TCA GTT GAA CTC CA -3', UPF1 forward primer 5'- CTG CAA CGG ACG
336 TGG AAA TAC -3', UPF1 reverse primer 5'- ACA GCC GCA GTT GTA GCA C -3', DDIT3
337 forward primer 5'- CTG CTT CTC TGG CTT GGC TG -3', DDIT3 reverse primer 5'- GCT
338 CTG GGA GGT GCT TGT GA -3', GADD45A forward primer 5'- GAG CTC CTG CTC
339 TTG GAG AC -3', GADD45A reverse primer 5'- GCA GGA TCC TTC CAT TGA GA -3',
340 GADD45B forward primer 5'- TGA CAA CGA CAT CAA CAT C -3', and GADD45B reverse
341 primer 5'- GTG ACC AGA GAC AAT GCA G -3'. Relative levels of each transcript were

342 normalized by the delta threshold cycle method to the abundance of 18S rRNA or
343 GAPDH, with mock-infected cells or vector-transfected cells set to 1.
344
345 **Western blot analysis.** Cells were lysed in RIPA lysis buffer (50 mM Tris-HCl, pH 8, 150
346 mM NaCl, 1% NP-40, 0.5% sodium deoxycholate, 0.1% SDS, supplemented with Halt™
347 protease inhibitor cocktail (ThermoFisher Scientific)) to obtain whole cell lysates or lysed
348 using the NE-PER nuclear and cytoplasmic extraction kit (ThermoFisher Scientific) to
349 obtain cytoplasmic and nuclear fractions. Proteins were separated by SDS-PAGE and
350 transferred to nitrocellulose membranes (Bio-Rad). Blots were incubated with the
351 indicated primary antibody: anti-UPF3B (ab134566, Abcam), anti-UPF1 (12040, Cell
352 Signaling Technology, Inc.), anti-ZIKV Capsid (C) (GTX133304, GeneTex), anti-Flag
353 (F7425, Sigma-Aldrich), anti-β-actin (A5316, Sigma-Aldrich), anti-ZIKV Envelope (E)
354 (GTX133314, GeneTex), anti-SP1 (sc-14027, Santa Cruz Biotechnology), anti-GAPDH
355 (5174, Cell Signaling Technology, Inc.), anti-Myc tag (ab9106, Abcam), anti-Strep tag
356 (ab18422, Abcam), and anti-p62 (ab56416, Abcam). Proteins were visualized by
357 chemiluminescent detection with ECL and ECL Hyperfilm (Amersham). Differences in
358 band intensity were quantified by densitometry using ImageJ.
359
360 **Immunoprecipitations.** Cells were lysed in either RIPA lysis buffer or IP lysis buffer
361 (150mM NaCl, 50mM Tris pH 7.4, 1mM EDTA, 0.5% NP-40 substitute, supplemented
362 with Halt™ protease inhibitor cocktail (ThermoFisher Scientific) at 4°C and passed
363 through a G23 needle. Clarified lysates were immunoprecipitated with Flag M2 agarose

364 (Sigma), anti-Myc tag (ab9106, Abcam), or normal rabbit IgG (sc-2027, Santa Cruz
365 Biotechnology) overnight, washed in lysis buffer, and resuspended in Laemmli buffer for
366 SDS-PAGE. Western blot analysis of immunoprecipitated proteins was performed as
367 described above.
368
369 **Immunofluorescence.** Transfected Huh7-Lunet cells or infected NPCs were collected at
370 48 h and plated onto 22 × 22 mm #1.5 coverslips. Cells were fixed in 4%
371 paraformaldehyde, permeabilized with 0.1% Triton X-100, and blocked in 3% bovine
372 serum albumin. Cells were then immunostained with the indicated antibodies: anti-Strep
373 Tag (Abcam, ab184224), anti-UPF1 (Abcam, ab109363), human anti-DENV mAb 1.6D
374 (Sharon Isern and Scott Michael, Florida Gulf Coast University), which recognizes the
375 ZIKV envelope protein, anti-dsRNA mAb J2 (SCICONS), and the appropriate fluorophore-
376 conjugated secondary antibodies. Coverslips were mounted onto glass slides using
377 Vectashield® Mounting Medium with DAPI (Vector Laboratories) and analyzed by
378 fluorescence microscopy (Zeiss Axio Observer ZI) or confocal microscopy (Zeiss LSM
379 880). For acquiring high-resolution images, cells were imaged on the Zeiss LSM 880 with
380 Airyscan using a 20x/0.8 or 63x/1.4 M27 oil immersion objective. A total of 15-20 (20x
381 objective) or 60-80 (63x objective) Z-slices were acquired every 0.88 μm or 0.15 μm,
382 respectively. The resulting Z-stack was reconstructed and rendered in 3D using Imaris
383 software (Bitplane). Viral dsRNA foci were reconstructed via the Imaris spot detection
384 function, which provided an analysis of total number and mean volume of foci within a
385 cell, for images acquired using the 20x objective. Strep-tagged ZIKV capsid, UPF1, and

386 dsRNA channels acquired using the 63x objective were reconstructed using the Imaris
387 surfaces package. The Imaris colocalization function was used to determine overlap of
388 fluorescence. Thresholding for background fluorescence was determined by the Imaris
389 automatic thresholding tool that utilizes the Costes approach (54). The thresholded
390 Mander's correlation coefficient (MCC) measures the fraction of voxels with fluorescence
391 positive for one channel that also contain fluorescence from another channel. The MCC
392 is typically more appropriate for analysis of three-dimensional colocalization (55).
393
394 **Statistical analysis.** Statistical differences between groups were analyzed using either
395 a two-tailed unpaired Student's *t*-test or a two-tailed ratio paired Student's *t*-test, as stated
396 in the figure legends. Hypergeometrical tests were used to calculate the probability of an
397 overlap in gene dysregulation between ZIKV-infected NPCs and UPF1-depleted cells and
398 to calculate the probability of ZIKV capsid bait-prey interactions. Data are represented as
399 mean ± s.e.m. Statistical significance was defined as $^{*}P \leq 0.05$, $^{**}P \leq 0.01$, $^{***}P \leq 0.001$,
400 and $^{****}P \leq 0.0001$.
401
402 **Acknowledgements.** The authors would like to thank all members of the Ott laboratory,
403 as well as Roman Camarda, Marius Walter, and Anna Maurer for helpful discussions and
404 advice throughout the preparation of this manuscript. We thank Chia-Lin Tsou, the
405 Gladstone Stem Cell Core, and Meredith Calvert from the Gladstone Microscopy Core for
406 technical assistance, and Ralf Bartenschlager (Heidelberg University), Lynne Maquat
407 (University of Rochester), and Sharon Isern and Scott Michael (Florida Gulf Coast

University) for reagents. We are grateful to Veronica Fonseca for administrative support, John Carroll and Teresa Roberts for graphical design, and to Kathryn Claiborn, Eric Martens, and Gary Howard for editorial assistance. This work was supported by NIH/NIAID F32AI112262 to P.S.S., NIH/NINDS R01 NS101996-01 to S.F., NIH/NIAID U19AI1186101 to N.J.K., DOD/DARPA HR0011-11-C-0094 (PROPHECY) to N.J.K., NIH/NIAID R01 AI097552 to M.O., and the James B. Pendleton Charitable Trust.

416 **References**

417 1. Fauci AS, Morens DM. 2016. Zika Virus in the Americas--Yet Another Arbovirus Threat.
418 N Engl J Med 374:601-604. 10.1056/NEJMp1600297.
419 2. Cugola FR, Fernandes IR, Russo FB, Freitas BC, Dias JLM, Guimarães KP, Benazzato
420 C, Almeida N, Pignatari GC, Romero S, Polonio CM, Cunha I, Freitas CL, Brandão WN,
421 Rossato C, Andrade DG, Faria DdP, Garcez AT, Buchpigel CA, Braconi CT, Mendes E,
422 Sall AA, Zanotto, Paolo M. de A., Peron JPS, Muotri AR, Beltrão-Braga PCB. 2016. The
423 Brazilian Zika virus strain causes birth defects in experimental models. Nature 534:267-
424 271. 10.1038/nature18296.
425 3. Shao Q, Herrlinger S, Yang S, Lai F, Moore JM, Brindley MA, Chen J. 2016. Zika virus
426 infection disrupts neurovascular development and results in postnatal microcephaly with
427 brain damage. Development 143:4127-4136. 10.1242/dev.143768.
428 4. Souza BSF, Sampaio GLA, Pereira CS, Campos GS, Sardi SI, Freitas LAR, Figueira
429 CP, Paredes BD, Nonaka CKV, Azevedo CM, Rocha VPC, Bandeira AC, Mendez-Otero
430 R, Dos Santos RR, Soares MBP. 2016. Zika virus infection induces mitosis abnormalities
431 and apoptotic cell death of human neural progenitor cells. Scientific reports 6:39775.
432 10.1038/srep39775.
433 5. Li C, Xu D, Xu Z, Ye Q, Hong S, Jiang Y, Liu X, Zhang N, Shi L, Qin C. 2016. Zika
434 Virus Disrupts Neural Progenitor Development and Leads to Microcephaly in Mice. Cell
435 Stem Cell 19:120-126. 10.1016/j.stem.2016.04.017.
436 6. Tang H, Hammack C, Ogden S, Wen Z, Qian X, Li Y, Yao B, Shin J, Zhang F, Lee E,
437 Christian K, Didier R, Jin P, Song H, Ming G. 2016. Zika Virus Infects Human Cortical

438 Neural Progenitors and Attenuates Their Growth. Cell Stem Cell 18:587-590.
439 10.1016/j.stem.2016.02.016.
440 7. Sonja A Rasmussen, Denise J Jamieson, Margaret A Honein, Lyle R Petersen. 2016.
441 Zika Virus and Birth Defects--Reviewing the Evidence for Causality. The New England
442 journal of medicine 374:1981-1987. 10.1056/NEJMsr1604338.
443 8. Harris E, Holden KL, Edgil D, Polacek C, Clyde K. 2006. Molecular biology of
444 flaviviruses. Novartis Found Symp 277:253.
445 9. Lindenbach BD, Rice CM. 2003. Molecular biology of flaviviruses. Adv Virus Res 59:23-
446 61.
447 10. Oliveira ERA, Mohana-Borges R, de Alencastro RB, Horta BAC. 2017. The flavivirus
448 capsid protein: Structure, function and perspectives towards drug design. Virus Res
449 227:115-123. 10.1016/j.virusres.2016.10.005.
450 11. den Boon JA, Diaz A, Ahlquist P. 2010. Cytoplasmic Viral Replication Complexes.
451 Cell Host Microbe 8:77-85. 10.1016/j.chom.2010.06.010.
452 12. Colpitts TM, Barthel S, Wang P, Fikrig E. 2011. Dengue virus capsid protein binds
453 core histones and inhibits nucleosome formation in human liver cells. PLoS ONE
454 6:e24365. 10.1371/journal.pone.0024365.
455 13. Lukasz P Slomnicki, Dong-Hoon Chung, Austin Parker, Taylor Hermann, Nolan L
456 Boyd, Michal Hetman. 2017. Ribosomal stress and Tp53-mediated neuronal apoptosis in
457 response to capsid protein of the Zika virus. Scientific Reports (Nature Publisher Group)
458 7:1-15. 10.1038/s41598-017-16952-8.

459 14. Tsuda Y, Mori Y, Abe T, Yamashita T, Okamoto T, Ichimura T, Moriishi K, Matsuura
460 Y. 2006. Nucleolar protein B23 interacts with Japanese encephalitis virus core protein
461 and participates in viral replication. Microbiol Immunol 50:225-234.
462 15. Xu Z, Hobman TC. 2012. The helicase activity of DDX56 is required for its role in
463 assembly of infectious West Nile virus particles. Virology 433:226-235.
464 10.1016/j.virol.2012.08.011.
465 16. Rawlinson SM, Moseley GW. 2015. The nucleolar interface of RNA viruses. Cell
466 Microbiol 17:1108-1120. 10.1111/cmi.12465.
467 17. Peccarelli M, Kebaara BW. 2014. Regulation of natural mRNAs by the nonsense-
468 mediated mRNA decay pathway. Eukaryotic cell 13:1126-1135. 10.1128/EC.00090-14.
469 18. Hug N, Longman D, Cáceres JF. 2016. Mechanism and regulation of the nonsense-
470 mediated decay pathway. Nucleic Acids Res 44:1483-1495. 10.1093/nar/gkw010.
471 19. Han X, Wei Y, Wang H, Wang F, Ju Z, Li T. 2018. Nonsense-mediated mRNA decay:
472 a 'nonsense' pathway makes sense in stem cell biology. Nucleic acids research 46:1038-
473 1051. 10.1093/nar/gkx1272.
474 20. Silver DL, Watkins-Chow DE, Schreck KC, Pierfelice TJ, Larson DM, Burnetti AJ, Liaw
475 H, Myung K, Walsh CA, Gaiano N, Pavan WJ. 2010. The exon junction complex
476 component Magoh controls brain size by regulating neural stem cell division. Nat
477 Neurosci 13:551-558. 10.1038/nn.2527.
478 21. Mao H, Pilaz L, McMahon JJ, Golzio C, Wu D, Shi L, Katsanis N, Silver DL. 2015.
479 Rbm8a haploinsufficiency disrupts embryonic cortical development resulting in
480 microcephaly. J Neurosci 35:7003-7018. 10.1523/JNEUROSCI.0018-15.2015.

481 22. Mao H, McMahon JJ, Tsai Y, Wang Z, Silver DL. 2016. Haploinsufficiency for Core
482 Exon Junction Complex Components Disrupts Embryonic Neurogenesis and Causes
483 p53-Mediated Microcephaly. PLoS Genetics 12:e1006282.
484 10.1371/journal.pgen.1006282.
485 23. Kurosaki T, Maquat LE. 2016. Nonsense-mediated mRNA decay in humans at a
486 glance. J Cell Sci 129:461-467. 10.1242/jcs.181008.
487 24. Serquiña AKP, Das SR, Popova E, Ojelabi OA, Roy CK, Göttlinger HG. 2013. UPF1
488 is crucial for the infectivity of human immunodeficiency virus type 1 progeny virions. J
489 Virol 87:8853-8861. 10.1128/JVI.00925-13.
490 25. Jerome M Molleston, Sara Cherry. 2017. Attacked from All Sides: RNA Decay in
491 Antiviral Defense. Viruses 9:2. 10.3390/v9010002.
492 26. Balistreri G, Bognanni C, Mühlemann O. 2017. Virus Escape and Manipulation of
493 Cellular Nonsense-Mediated mRNA Decay. Viruses 9:. 10.3390/v9010024.
494 27. Rigby RE, Rehwinkel J. 2015. RNA degradation in antiviral immunity and
495 autoimmunity. Trends in Immunology 36:179-188. 10.1016/j.it.2015.02.001.
496 28. Balistreri G, Horvath P, Schweingruber C, Zünd D, McInerney G, Merits A,
497 Mühlemann O, Azzalin C, Helenius A. 2014. The host nonsense-mediated mRNA decay
498 pathway restricts Mammalian RNA virus replication. Cell Host Microbe 16:403-411.
499 10.1016/j.chom.2014.08.007.
500 29. Ramage HR, Kumar GR, Verschueren E, Johnson JR, Von Dollen J, Johnson T,
501 Newton B, Shah P, Horner J, Krogan NJ, Ott M. 2015. A combined proteomics/genomics

502 approach links hepatitis C virus infection with nonsense-mediated mRNA decay. Mol Cell
503 57:329-340. 10.1016/j.molcel.2014.12.028.
504 30. Tani H, Imamachi N, Salam KA, Mizutani R, Ijiri K, Irie T, Yada T, Suzuki Y, Akimitsu
505 N. 2012. Identification of hundreds of novel UPF1 target transcripts by direct
506 determination of whole transcriptome stability. RNA Biology 9:1370-1379.
507 10.4161/rna.22360.
508 31. Weischenfeldt J, Damgaard I, Bryder D, Theilgaard-Mönch K, Thoren LA, Nielsen FC,
509 Jacobsen SEW, Nerlov C, Porse BT. 2008. NMD is essential for hematopoietic stem and
510 progenitor cells and for eliminating by-products of programmed DNA rearrangements.
511 Genes Dev 22:1381-1396. 10.1101/gad.468808.
512 32. Li T, Shi Y, Wang P, Guachalla LM, Sun B, Joerss T, Chen Y, Groth M, Krueger A,
513 Platzer M, Yang Y, Rudolph KL, Wang Z. 2015. Smg6/Est1 licenses embryonic stem cell
514 differentiation via nonsense-mediated mRNA decay. EMBO J 34:1630-1647.
515 10.15252/embj.201489947.
516 33. Brazão TF, Demmers J, van IJcken W, Strouboulis J, Fornerod M, Romão L, Grosveld
517 FG. 2012. A new function of ROD1 in nonsense-mediated mRNA decay. FEBS Lett
518 586:1101-1110. 10.1016/j.febslet.2012.03.015.
519 34. Chan W, Huang L, Gudikote JP, Chang Y, Imam JS, MacLean JA, Wilkinson MF.
520 2007. An alternative branch of the nonsense-mediated decay pathway. EMBO J 26:1820-
521 1830. 10.1038/sj.emboj.7601628.

522 35. Nelson JO, Moore KA, Chapin A, Hollien J, Metzstein MM. 2016. Degradation of
523 Gadd45 mRNA by nonsense-mediated decay is essential for viability. Elife 5:.
524 10.7554/eLife.12876.
525 36. Jauhiainen A, Thomsen C, Strömbom L, Grundevik P, Andersson C, Danielsson A,
526 Andersson MK, Nerman O, Rörkvist L, Ståhlberg A, Åman P. 2012. Distinct cytoplasmic
527 and nuclear functions of the stress induced protein DDIT3/CHOP/GADD153. PLoS ONE
528 7:e33208. 10.1371/journal.pone.0033208.
529 37. Salvador JM, Brown-Clay JD, Fornace AJ. 2013. Gadd45 in stress signaling, cell cycle
530 control, and apoptosis. Adv Exp Med Biol 793:1-19. 10.1007/978-1-4614-8289-5_1.
531 38. Gehring NH, Lamprinaki S, Kulozik AE, Hentze MW. 2009. Disassembly of exon
532 junction complexes by PYM. Cell 137:536-548. 10.1016/j.cell.2009.02.042.
533 39. Chamieh H, Ballut L, Bonneau F, Le Hir H. 2008. NMD factors UPF2 and UPF3 bridge
534 UPF1 to the exon junction complex and stimulate its RNA helicase activity. Nat Struct Mol
535 Biol 15:85-93. 10.1038/nsmb1330.
536 40. Varsally W, Brogna S. 2012. UPF1 involvement in nuclear functions. Biochem Soc
537 Trans 40:778-783. 10.1042/BST20120052.
538 41. Klema VJ, Padmanabhan R, Choi KH. 2015. Flaviviral Replication Complex:
539 Coordination between RNA Synthesis and 5′-RNA Capping. Viruses 7:4640-4656.
540 10.3390/v7082837.
541 42. Maisel M, Herr A, Milosevic J, Hermann A, Habisch H, Schwarz S, Kirsch M,
542 Antoniadis G, Brenner R, Hallmeyer-Elgner S, Lerche H, Schwarz J, Storch A. 2007.
543 Transcription profiling of adult and fetal human neuroprogenitors identifies divergent

544 paths to maintain the neuroprogenitor cell state. Stem Cells 25:1231-1240.
545 10.1634/stemcells.2006-0617.
546 43. Li H, Saucedo-Cuevas L, Regla-Nava J, Chai G, Sheets N, Tang W, Terskikh A,
547 Shresta S, Gleeson J. 2016. Zika Virus Infects Neural Progenitors in the Adult Mouse
548 Brain and Alters Proliferation. Cell Stem Cell 19:593-598. 10.1016/j.stem.2016.08.005.
549 44. Nickless A, Bailis JM, You Z. 2017. Control of gene expression through the nonsense-
550 mediated RNA decay pathway. Cell & Bioscience 7:1-12. 10.1186/s13578-017-0153-7.
551 45. Cortese M, Goellner S, Acosta EG, Neufeldt CJ, Oleksiuk O, Lampe M, Haselmann
552 U, Funaya C, Schieber N, Ronchi P, Schorb M, Pruunsild P, Schwab Y, Chatel-Chaix L,
553 Ruggieri A, Bartenschlager R. 2017. Ultrastructural Characterization of Zika Virus
554 Replication Factories. Cell Rep 18:2113-2123. 10.1016/j.celrep.2017.02.014.
555 46. Grant A, Ponia SS, Tripathi S, Balasubramaniam V, Miorin L, Sourisseau M, Schwarz
556 MC, Sánchez-Seco MP, Evans MJ, Best SM, García-Sastre A. 2016. Zika Virus Targets
557 Human STAT2 to Inhibit Type I Interferon Signaling. Cell Host Microbe 19:882-890.
558 10.1016/j.chom.2016.05.009.
559 47. von Mikecz A. 2006. The nuclear ubiquitin-proteasome system. J Cell Sci 119:1977-
560 1984. 10.1242/jcs.03008.
561 48. Freire JM, Veiga AS, Conceição TM, Kowalczyk W, Mohana-Borges R, Andreu D,
562 Santos NC, Da Poian AT, Castanho, Miguel A. R. B. 2013. Intracellular nucleic acid
563 delivery by the supercharged dengue virus capsid protein. PLoS ONE 8:e81450.
564 10.1371/journal.pone.0081450.

565 49. HD iPSC Consortium. 2017. Developmental alterations in Huntington's disease neural
566 cells and pharmacological rescue in cells and mice. Nat Neurosci 20:648-660.
567 10.1038/nn.4532.
568 50. Jäger S, Gulbahce N, Cimermancic P, Kane J, He N, Chou S, D'Orso I, Fernandes J,
569 Jang G, Frankel AD, Alber T, Zhou Q, Krogan NJ. 2011. Purification and characterization
570 of HIV-human protein complexes. Methods 53:13-19. 10.1016/j.ymeth.2010.08.007.
571 51. Cox J, Hein MY, Luber CA, Paron I, Nagaraj N, Mann M. 2014. Accurate proteome-
572 wide label-free quantification by delayed normalization and maximal peptide ratio
573 extraction, termed MaxLFQ. Mol Cell Proteomics 13:2513-2526.
574 10.1074/mcp.M113.031591.
575 52. Cox J, Mann M. 2008. MaxQuant enables high peptide identification rates,
576 individualized p.p.b.-range mass accuracies and proteome-wide protein quantification.
577 Nat Biotechnol 26:1367-1372. 10.1038/nbt.1511.
578 53. Teo G, Koh H, Fermin D, Lambert J, Knight JDR, Gingras A, Choi H. 2016. SAINTq:
579 Scoring protein-protein interactions in affinity purification - mass spectrometry
580 experiments with fragment or peptide intensity data. Proteomics 16:2238-2245.
581 10.1002/pmic.201500499.
582 54. Costes SV, Daelemans D, Cho EH, Dobbin Z, Pavlakis G, Lockett S. 2004. Automatic
583 and quantitative measurement of protein-protein colocalization in live cells. Biophys J
584 86:3993-4003. 10.1529/biophysj.103.038422.

585 55. Dunn KW, Kamocka MM, McDonald JH. 2011. A practical guide to evaluating
586 colocalization in biological microscopy. Am J Physiol Cell Physiol 300:C742.
587 10.1152/ajpcell.00462.2010.
588 56. Paul LM, Carlin ER, Jenkins MM, Tan AL, Barcellona CM, Nicholson CO, Michael SF,
589 Isern S. 2016. Dengue virus antibodies enhance Zika virus infection. Clinical &
590 Translational Immunology 5:n/a. 10.1038/cti.2016.72.
591
592
593
594
595
596
597
598
599
600
601
602
603
604
605
606

607 **Figure Legends**

608 **Figure 1. ZIKV infection disrupts the NMD pathway.**

609 (a) Transcript levels of NMD substrates and housekeeping genes from Huh7 cells or
610 NPCs mock-infected or infected with ZIKV strain P6-740 or the contemporary clinical
611 isolate PRVABC59. Cells were infected at a multiplicity of infection (MOI) of 0.1 or 1 and
612 harvested at 48 hpi. Data are represented as mean ± s.e.m. *P* values were calculated by
613 unpaired Student's *t*-test. **P* ≤ 0.05; ***P* ≤ 0.01; ns, not significant. n= 3 independent
614 experiments.

615 (b) Venn diagram showing overlap of significantly upregulated genes associated with
616 ZIKV infection of NPCs and UPF1 knockdown in HeLa cells. RNA-Seq analyses of mock-
617 infected or ZIKV-infected NPCs harvested at 56 hpi and control siRNA-treated or UPF1
618 siRNA-treated HeLa TO cells harvested at 72 h post-transfection (hpt). The GeneProf
619 hypergeometric probability calculator was then used to generate a hypergeometric *P*
620 value. *****P* ≤ 0.0001.

621 (c) Transcript levels of housekeeping genes and select genes involved in cell cycle growth
622 arrest and apoptosis that were identified in (b). Huh7 cells were mock-infected or infected
623 with ZIKV PRVABC59 at an MOI of 0.1 or 1 and harvested at 48 hpi. Data are represented
624 as mean ± s.e.m. *P* values were calculated by unpaired Student's *t*-test. **P* ≤ 0.05; ***P* ≤
625 0.01; ****P* ≤ 0.001; ns, not significant. n= 3 independent experiments.

626

627

628

629 **Figure 2. The capsid protein of ZIKV interacts with the NMD pathway.**

630 (a) Ugandan ZIKV capsid (Ug Cap, MR 766) and French Polynesian ZIKV capsid (Fp
631 Cap, H/PF/2013) PPI maps that show significant enrichment for host NMD-associated
632 factors (purple), as identified by AP-MS (SAINTq probability score > 0.9 and FDR < 0.05).
633 Ten interactions between Fp Cap and host NMD factors (hypergeometrical test, *P* value
634 = 7.16×10^{-10}) and eight interactions between Ug Cap and host NMD factors (*P* value =
635 3.45×10^{-7}) were identified.

636 (b) Co-immunoprecipitation (co-IP) and western blot analysis of HEK293T cells
637 transfected with vector or Flag-tagged ZIKV capsid (H/PF/2013, Asian lineage) and
638 harvested at 48 hpt to immunoprecipitate endogenous UPF3B. The upper band detected
639 in the IP Capsid blot represents a non-specific artifact.

640 (c) Co-IP and western blot analysis of HEK293T cells transfected with vector or Flag-
641 tagged ZIKV capsid and harvested at 48 hpt to immunoprecipitate endogenous UPF1.

642 (d) Myc-tag co-IP and western blot analysis of HEK293T cells transfected with Strep-
643 tagged ZIKV capsid and Myc-UPF1 (WT), Myc-UPF1-C126S (RNA-binding mutant), or
644 Myc-UPF1-G495R/G497E (ATPase/helicase mutant) and harvested at 48 hpt to
645 immunoprecipitate ZIKV capsid.

646 (e) Western blot analysis of UPF1 levels in mock-infected and ZIKV-infected (PRVABC59,
647 MOI of 1) Huh7 cells or mock-infected and ZIKV-infected (P6-740, MOI of 1) NPCs
648 harvested at 48 hpi, with β-actin and ZIKV envelope (ZIKV E) or ZIKV capsid (ZIKV C)
649 protein serving as loading and infection controls, respectively. Densitometric analyses
650 were performed using ImageJ to quantify relative band intensities. Data are represented

651 as mean ± s.e.m. *P* values were calculated by unpaired Student's *t*-test. ***P* ≤ 0.01; ****P*
652 ≤ 0.001. n= 3 independent experiments.
653
654 **Figure 3. ZIKV capsid degrades UPF1, the master regulator of NMD, via a**
655 **proteasome-dependent mechanism.**
656 (a) Western blot analysis of UPF1 levels in subcellular fractionated HEK293T cells
657 transfected with vector or Flag-tagged ZIKV capsid (H/PF/2013, Asian lineage) for 48 h.
658 GAPDH was used as a cytoplasmic marker and SP1 as a nuclear marker to ensure
659 optimal fractionation. Densitometric analyses were performed using ImageJ to quantify
660 relative band intensities. Data are represented as mean ± s.e.m. *P* values were calculated
661 by unpaired Student's *t*-test. ***P* ≤ 0.01; ns, not significant. n= 3 independent experiments.
662 (b) Western blot analysis of nuclear UPF1 levels in fractionated HEK293T cells
663 transfected with vector or Flag-tagged ZIKV capsid for 48 h. Cells were treated with
664 DMSO or increasing concentrations of the proteasome inhibitor bortezomib for 24 h
665 before harvest. Densitometric analyses were performed using ImageJ to quantify relative
666 band intensities. Data are represented as mean ± s.e.m. *P* values were calculated by
667 one-way ANOVA with multiple comparisons. **P* ≤ 0.05; ns, not significant. n= 3
668 independent experiments.
669 (c) Representative 3D confocal microscopy images of the nuclei of Huh7-Lunet cells
670 transfected with Strep-tagged ZIKV capsid. Cells were treated at 24 hpt with DMSO or 10
671 nM bortezomib and processed for immunostaining at 48 hpt with antibodies against Strep-
672 tag (turquoise) and endogenous UPF1 (purple). DAPI (blue) was used to stain and define

673 the nuclei. Each channel was reconstructed digitally for visualization of the 3D
674 colocalization. The thresholded Mander's correlation coefficients were determined and *P*
675 value was calculated by unpaired Student's *t*-test. $^{**}P \leq 0.01$. n = 8 cells per condition.
676 Scale bar represents 3 μm.
677
678 **Figure 4. UPF1 knockdown enhances the permissivity of NPCs to ZIKV infection.**
679 (a) Western blot analysis of UPF1 levels in NPCs transfected with non-targeting siRNA
680 (siNT) or a pool of UPF1-specific siRNAs (siUPF1) at 96 hpt. Densitometric analyses were
681 performed using ImageJ to quantify relative band intensities. Data are represented as
682 mean ± s.e.m. *P* value was calculated by unpaired Student's *t*-test. $^{**}P \leq 0.01$. n= 3
683 independent experiments using one NPC line.
684 (b) ZIKV RNA levels in siNT-treated or siUPF1-treated NPCs infected with ZIKV strain
685 PRVABC59 at an MOI of 0.1 or 1 and harvested at 48 hpi. Data are represented as mean
686 ± s.e.m. *P* value was calculated by two-tailed ratio paired Student's *t*-test. $^{***}P \leq 0.001$.
687 n= 3 independent experiments using one NPC line.
688 (c) Released infectious virus from siNT-treated or siUPF1-treated, ZIKV-infected (MOI of
689 1) NPCs harvested at 48 hpi. Data are represented as mean ± s.e.m. *P* value was
690 calculated by unpaired Student's *t*-test. $^{**}P \leq 0.01$. n= 3 independent experiments using
691 one NPC line.
692 (d) Representative confocal microscopy images of a ZIKV-infected, siNT-treated NPC or
693 a ZIKV-infected, siUPF1-treated NPC with the nuclei stained with DAPI (blue) and ZIKV
694 dsRNA foci stained with the anti-dsRNA mAb J2 (teal). 3D image rendering and

695 reconstructed dsRNA foci were produced using the Imaris spot detection function. Scale
696 bar represents 2 μm.
697 (e) Number of dsRNA foci were averaged for each cell. Data are represented as mean ±
698 s.e.m. *P* value was calculated by two-tailed ratio paired Student's *t*-test. ns, not significant.
699 n = 3 independent experiments using two NPC lines, with 3-10 cells analyzed per
700 condition for each experiment.
701 (f) Measurement of dsRNA foci volume were averaged for each cell. Data are represented
702 as mean ± s.e.m. *P* value was calculated by two-tailed ratio paired Student's *t*-test. ns,
703 not significant. n = 3 independent experiments using two NPC lines, with 3-10 cells
704 analyzed per condition for each experiment.
705 (g) Infection rates of siNT-treated or siUPF1-treated, ZIKV-infected (MOI of 1) NPCs
706 measured at 48 hpi. Fixed cells were subjected to the anti-DENV mAb 1.6D, which also
707 recognizes the ZIKV envelope protein (56). Data are represented as mean ± s.e.m. *P*
708 value was calculated by two-tailed ratio paired Student's *t*-test. $^{**}P \leq 0.01$. n = 3
709 independent experiments using two NPC lines.
710 (h) Model of the interaction between the capsid protein of ZIKV and UPF1 of the NMD
711 pathway.
712
713 **Supplemental Figure 1. UPF1 is not transcriptionally downregulated during ZIKV**
714 **infection or following ZIKV capsid overexpression.**
715 (a) UPF1 transcript levels from Huh7 cells mock-infected or infected with ZIKV strain
716 PRVABC59 at an MOI of 0.1 or 1 and harvested at 48 hpi. Data are represented as mean

717 ± s.e.m. *P* values were calculated by unpaired Student's *t*-test. ns, not significant. n= 3
718 independent experiments.
719 (b) UPF1 transcript levels from HEK293T cells transfected with vector or Strep-tagged
720 ZIKV capsid (H/PF/2013, Asian lineage) and harvested at 48 hpt. Data are represented
721 as mean ± s.e.m. *P* values were calculated by unpaired Student's *t*-test. ns, not
722 significant. n= 3 independent experiments.
723
724 **Supplemental Figure 2. ZIKV capsid-induced UPF1 degradation is not dependent**
725 **on autophagy.**
726 Western blot analysis of nuclear UPF1 levels in fractionated HEK293T cells transfected
727 with vector or Flag-tagged ZIKV capsid for 48 h. Cells were treated with DMSO or the
728 autophagy inhibitor bafilomycin A1 (Baf) (10 nM) for 24 h before harvest. Levels of p62,
729 which is degraded by autophagy, were monitored to confirm autophagic inhibition
730 following bafilomycin A1 treatment.
731
732 **Supplemental Figure 3. ZIKV capsid colocalizes with endogenous UPF1.**

733 Representative 3D confocal microscopy images of Huh7-Lunet cells transfected with vector or
734 Strep-tagged ZIKV capsid. Cells were processed for immunostaining at 48 hpt and probed with
735 antibodies against Strep-tag (turquoise) and endogenous UPF1 (purple). DAPI (blue) was used
736 to stain the nuclei. Each channel was reconstructed digitally for visualization of the 3D
737 colocalization. The thresholded Mander's correlation coefficient for ZIKV capsid was 0.57 (n =

738 17), indicating that approximately 57% of the voxels positive for capsid fluorescence were also

739 positive for UPF1 fluorescence. Scale bar represents 5 μm.

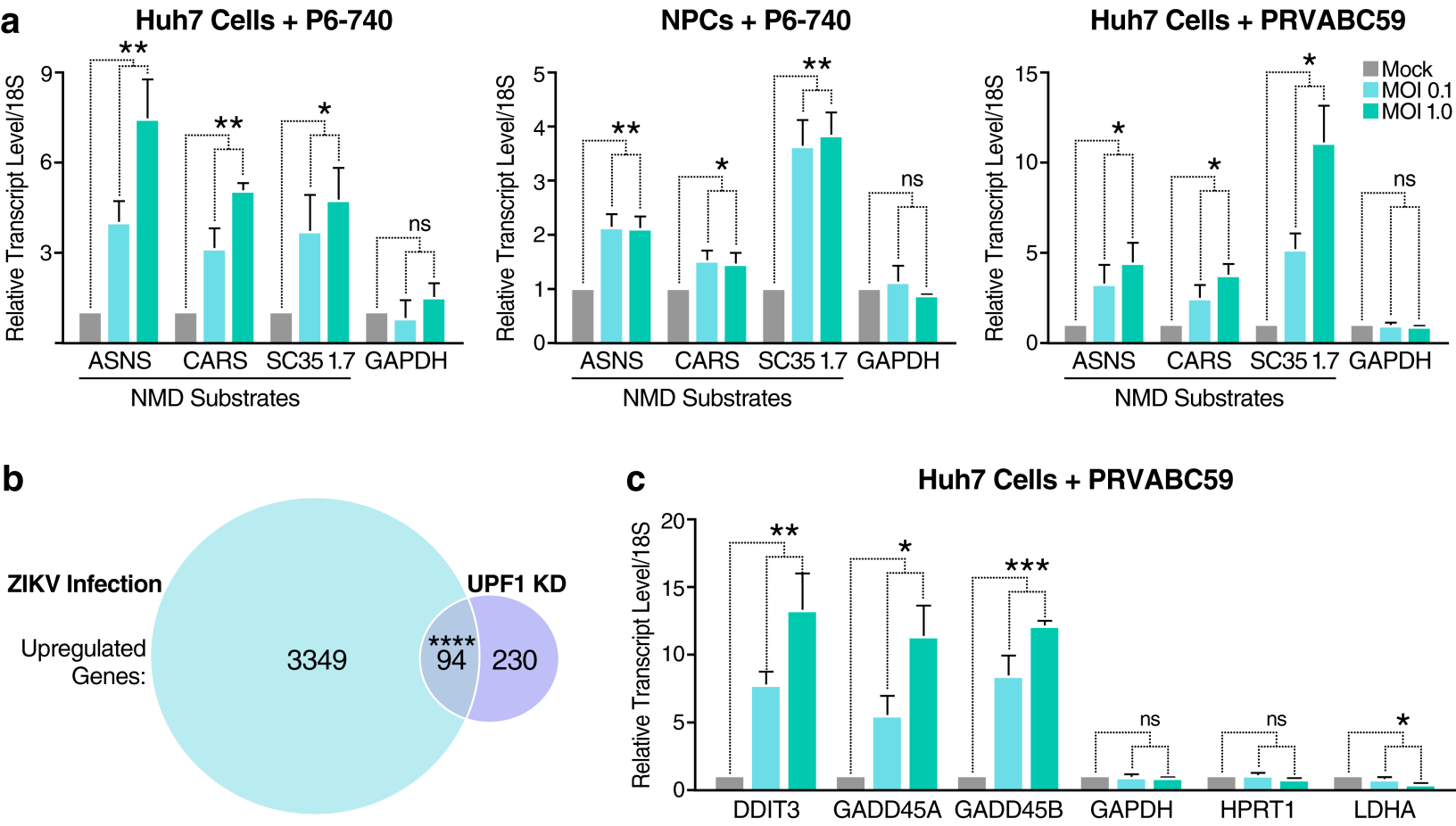
a
Huh7 Cells + P6-740
NPCs + P6-740
Huh7 Cells + PRVABC59
Relative Transcript Level/18S
Mock
MOI 0.1
MOI 1.0
ASNS
CARS
SC35 1.7
GAPDH
NMD Substrates
ns
b
ZIKV Infection
UPF1 KD
Upregulated Genes:
3349
****
94
230
c
Huh7 Cells + PRVABC59
DDIT3
GADD45A
GADD45B
GAPDH
HPRT1
LDHA

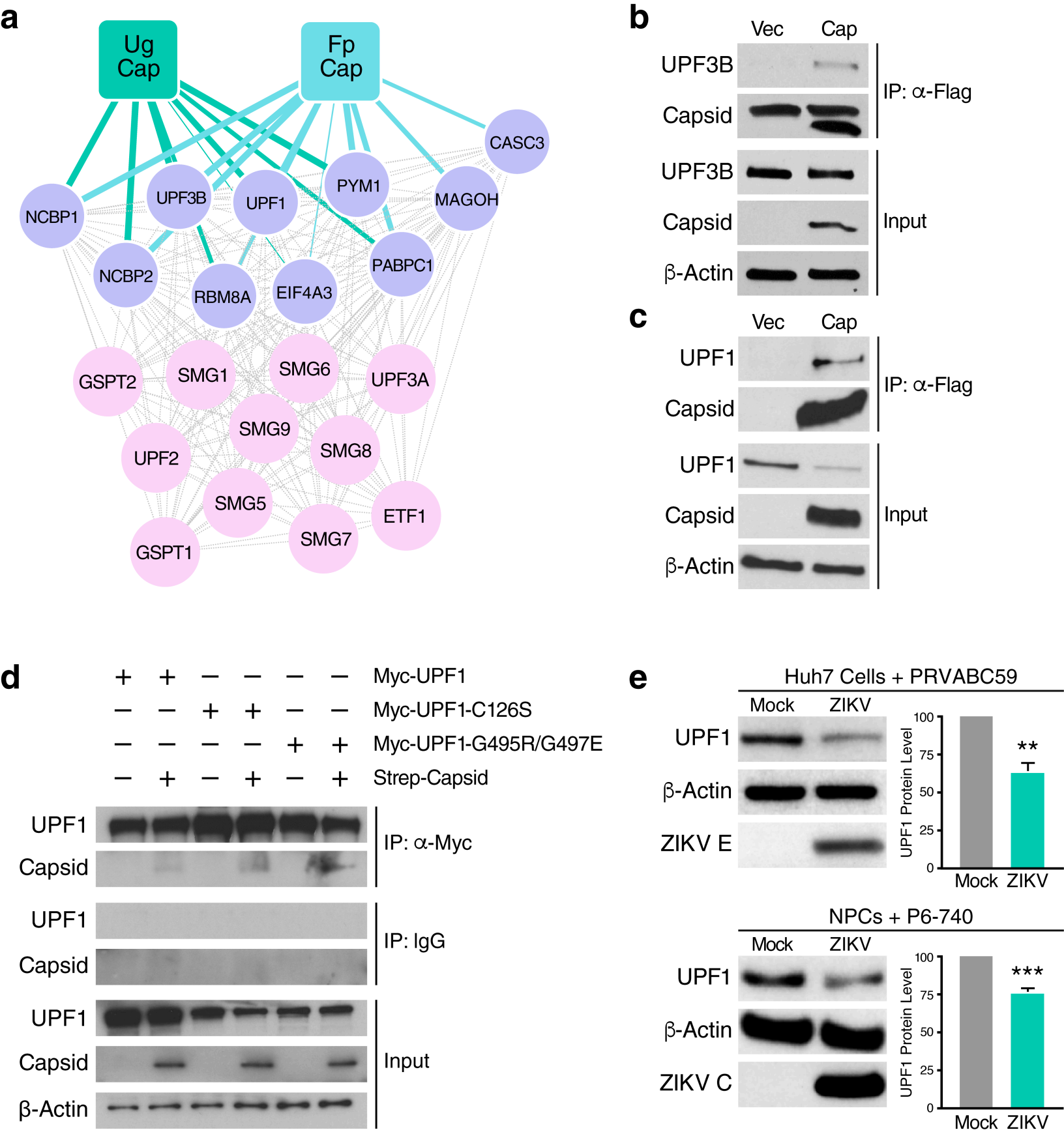
a
Ug Cap
Fp Cap
CASC3
NCBP1
UPF3B
UPF1
PYM1
MAGOH
NCBP2
RBM8A
EIF4A3
PABPC1
GSPT2
SMG1
SMG6
UPF3A
SMG9
UPF2
SMG8
SMG5
ETF1
GSPT1
SMG7
b
Vec
Cap
UPF3B
Capsid
IP: α-Flag
UPF3B
Capsid
β-Actin
Input
c
Vec
Cap
UPF1
Capsid
IP: α-Flag
UPF1
Capsid
β-Actin
Input
d
Myc-UPF1
Myc-UPF1-C126S
Myc-UPF1-G495R/G497E
Strep-Capsid
UPF1
Capsid
IP: α-Myc
UPF1
Capsid
IP: IgG
UPF1
Capsid
β-Actin
Input
e
Huh7 Cells + PRVABC59
Mock
ZIKV
UPF1
β-Actin
ZIKV E
UPF1 Protein Level
100
75
50
25
0
**
Mock
ZIKV
NPCs + P6-740
Mock
ZIKV
UPF1
β-Actin
ZIKV C
UPF1 Protein Level
100
75
50
25
0
***
Mock
ZIKV

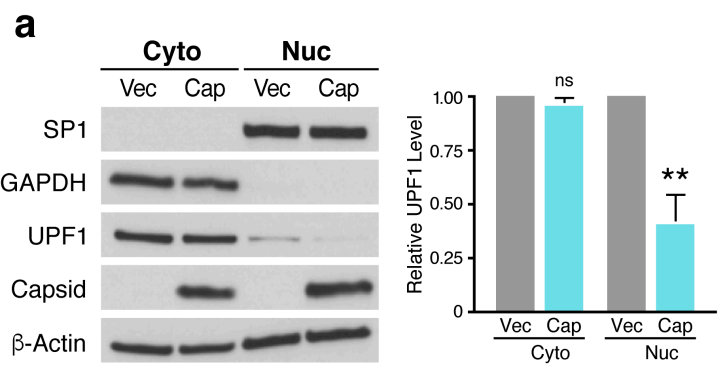
a
Cyto
Nuc
Vec
Cap
Vec
Cap
SP1
GAPDH
UPF1
Capsid
β-Actin
Relative UPF1 Level
1.00
0.75
0.50
0.25
0
ns
**
Vec
Cap
Vec
Cap
Cyto
Nuc

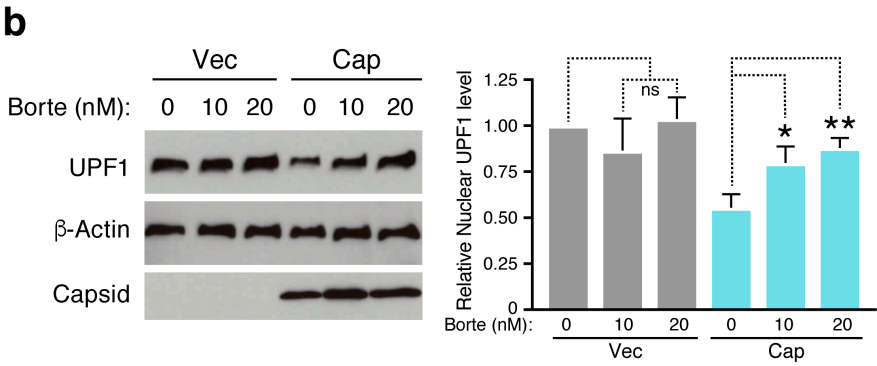
b
Vec
Cap
Borte (nM):
0
10
20
0
10
20
UPF1
β-Actin
Capsid
Relative Nuclear UPF1 level
1.25
1.00
0.75
0.50
0.25
0
ns
*
**
Borte (nM):
0
10
20
0
10
20
Vec
Cap

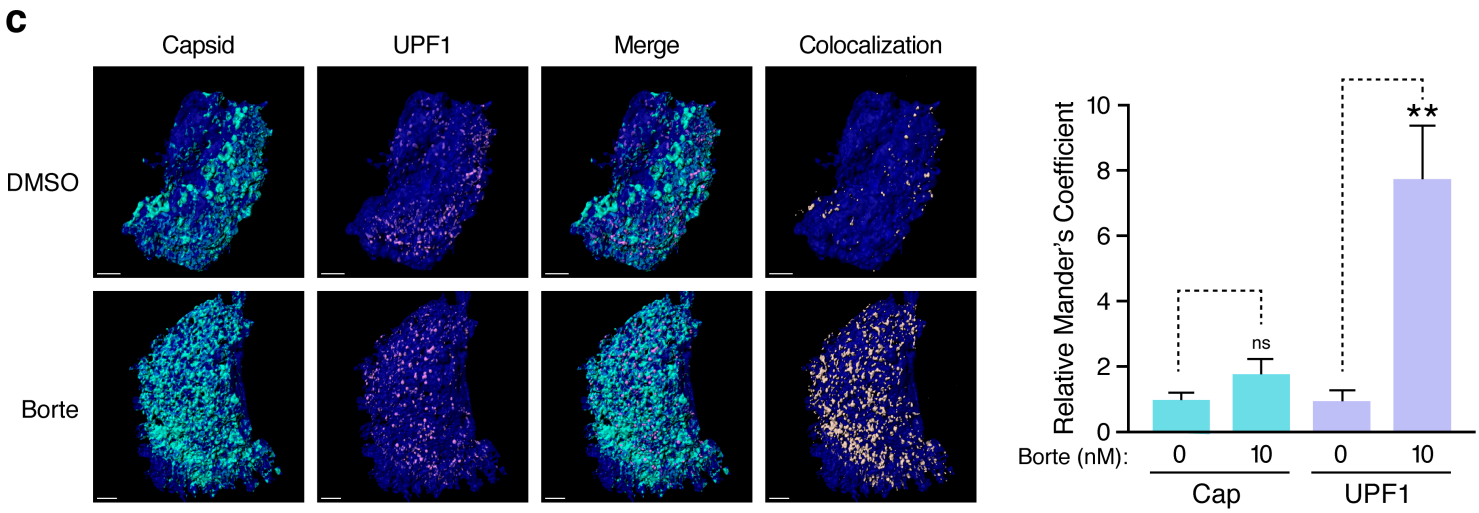
c
Capsid
UPF1
Merge
Colocalization
DMSO
Borte
Relative Mander's Coefficient
10
8
6
4
2
0
ns
**
Borte (nM):
0
10
0
10
Cap
UPF1

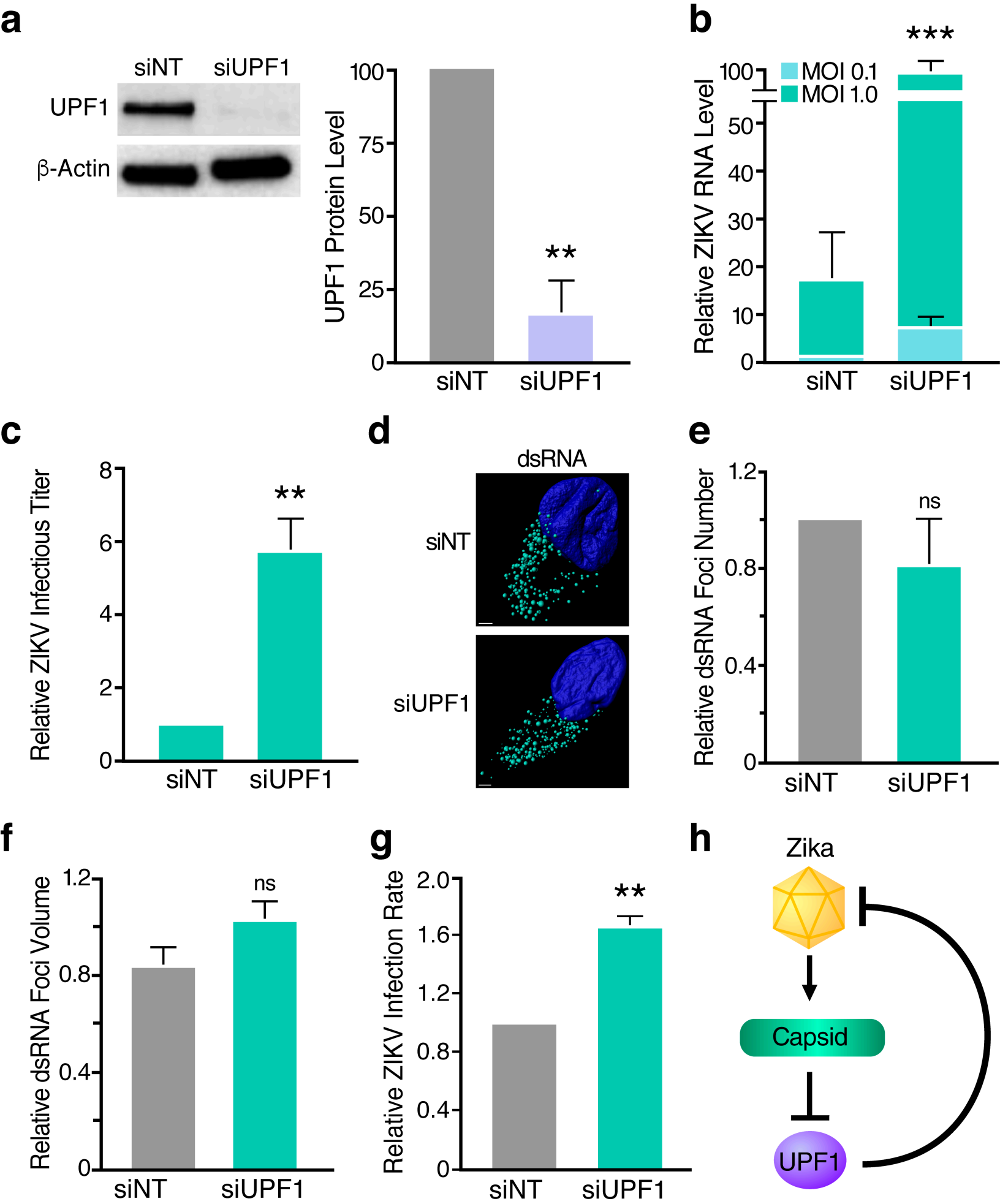
a
siNT
siUPF1
UPF1
β-Actin
UPF1 Protein Level
100
75
50
25
0
**
siNT
siUPF1
b
***
MOI 0.1
MOI 1.0
Relative ZIKV RNA Level
100
50
40
30
20
10
0
siNT
siUPF1
c
Relative ZIKV Infectious Titer
8
6
4
2
0
**
siNT
siUPF1
d
dsRNA
siNT
siUPF1
e
Relative dsRNA Foci Number
1.2
0.8
0.4
0
ns
siNT
siUPF1
f
Relative dsRNA Foci Volume
1.2
0.8
0.4
0
ns
siNT
siUPF1
g
Relative ZIKV Infection Rate
2.0
1.6
1.2
0.8
0.4
0
**
siNT
siUPF1
h
Zika
Capsid
UPF1

Supplementary Figure 1

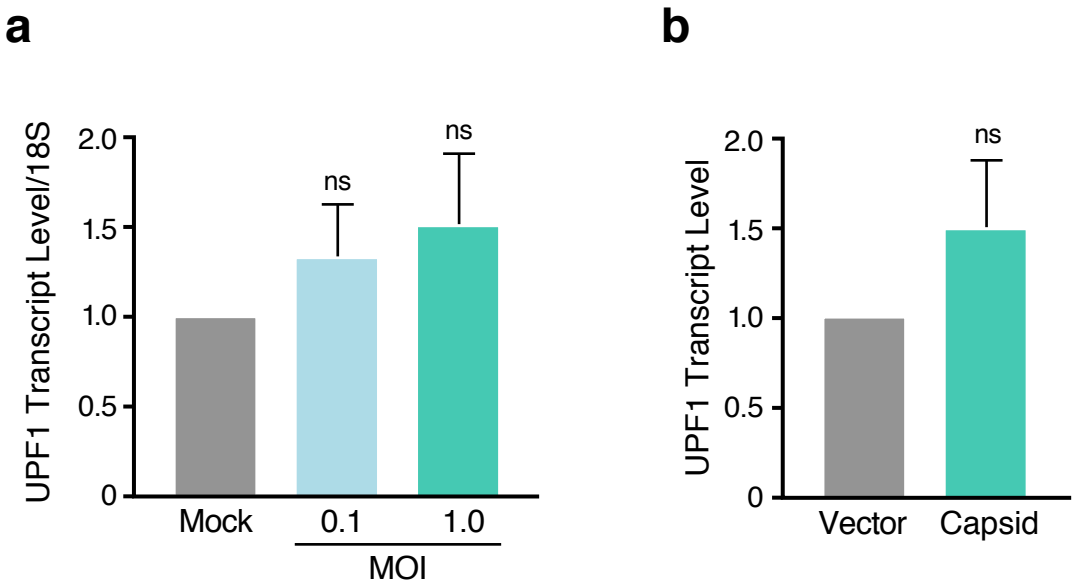

Supplementary Figure 2

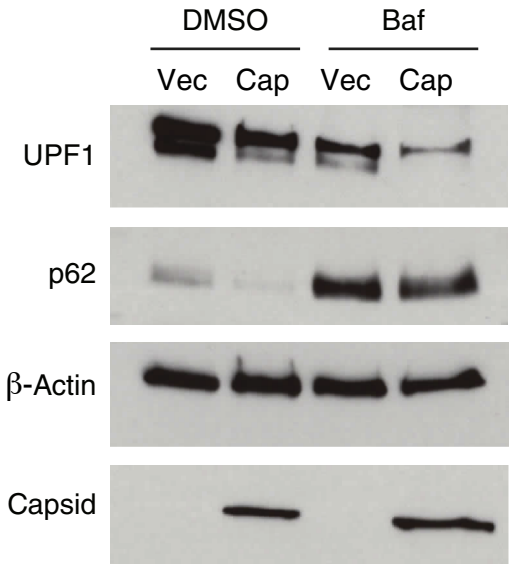
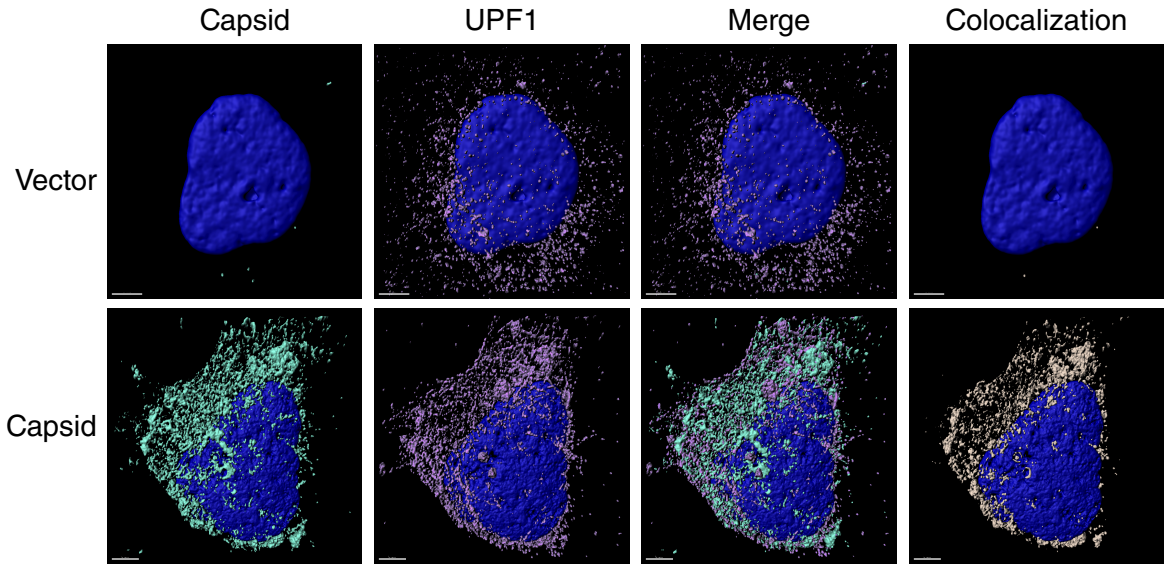
Supplementary Figure 3